

Discovering ABO_3 -type perovskite with different dielectric constants via intelligent optimization algorithm

Cite as: AIP Advances 14, 075012 (2024); doi: 10.1063/5.0210811

Submitted: 27 March 2024 • Accepted: 20 June 2024 •

Published Online: 10 July 2024



View Online



Export Citation



CrossMark

Taizhong Yao,¹ Lanping Chen,^{1,2,a} Nan Hu,² Lei Xu,¹ and Sichao Sun²

AFFILIATIONS

¹ School of Microelectronics and Control Engineering, Changzhou University, Changzhou 213159, Jiangsu, China

² School of Computer Science and Artificial Intelligence, Changzhou University, Changzhou 213159, Jiangsu, China

^aAuthor to whom correspondence should be addressed: chenlp@cczu.edu.cn

ABSTRACT

Nowadays, dielectric materials are playing an increasingly important role in various fields. A high dielectric constant (D) can store more charge per unit volume, improving performance, reducing device size, lowering D limit cross communication, and enabling better packaging of devices. Differentiating high D and low D has been recognized as a significant concern in electronics. However, calculating the dielectric constant (D) of different dielectric materials from first principles is notoriously difficult. Therefore, it is essential to find important descriptors for predicting the dielectric constant (D) of different dielectric materials. In this work, a novel intelligence optimization approach was proposed based on data-driven methods to predict the dielectric constant (D) of ABO_3 -type perovskites. By applying the machine learning (ML) algorithm, key features strongly correlated with D were identified. To reduce feature dimension, Random Forest Regression-Gradient Boosting Regressor (RFR-GBR) feature screening, sure independence screening, and the sparsifying operator approach were employed to compress the feature set for creating valid descriptors. Furthermore, the Shapley additive explanation technique was used to reveal the scaling relation between the dielectric constant and the identified descriptors for predicting the D of ABO_3 -type perovskites. In addition, a hybrid artificial rabbits optimization algorithm and random forest regression were developed for predicting D , achieving remarkable predictive performance with an R^2 score of 0.95, MAE of 0.23, and RMSE of 0.108 using five-fold cross-validation. Ultimately, from a pool of 300 candidate materials, we screened and identified two potential dielectric perovskites with different D values. The proposed framework will facilitate D prediction technology for the discovery of dielectric perovskite materials with favorable performance.

© 2024 Author(s). All article content, except where otherwise noted, is licensed under a Creative Commons Attribution-NonCommercial-NoDerivs 4.0 International (CC BY-NC-ND) license (<https://creativecommons.org/licenses/by-nc-nd/4.0/>). <https://doi.org/10.1063/5.0210811>

24 October 2024 18:08:53

I. INTRODUCTION

As electronic components become smaller and lighter, dielectric materials with different dielectric constants have emerged as a significant focus in the field of electronic materials. The dielectric constant (D) indicates the degree of polarization in an insulator without current flow.¹ For nearly half a century, dielectric materials have played a crucial role as core components in dielectric resonators, filters, and substrates for various applications, such as satellite television broadcasting, mobile communication, Bluetooth technology, radar, global positioning system (GPS), and other communication systems.² ABO_3 -type perovskites, as typical candidates for dielectric materials, possess unique electrical and magnetic

properties with different dielectric constants. It can be used for energy storage devices,³ solar cell equipment,⁴ and ceramic capacitors,⁵ including barium titanate (BaTiO_3)⁶ and strontium titanate (SrTiO_3).⁷ Consequently, the chemical or physical properties of dielectric materials associated with diverse D values have been extensively studied.

The precise prediction of D has become attractive research due to the diverse needs of dielectric materials for different applications.⁸ High D perovskite dielectric materials are suitable for energy storage in thin film capacitors,⁹ while low D perovskite dielectric materials are appropriate for insulation in power systems.¹⁰ When improving the dielectric properties of ABO_3 perovskites and developing cheaper and more efficient devices,¹¹ the traditional

trial-and-error method faces limitations due to experimental conditions and computational resources. Data-driven methods such as artificial intelligence (AI) techniques can be used to predict D by analyzing various features of the materials, such as structure, electrical characteristics, and thermal properties.¹² Machine learning (ML) can accelerate material property discovery, avoiding tedious testing and complex calculations,^{13,14} gaining attention in the field of materials science.¹⁵ Umeda *et al.*¹⁶ employed three regression models, LRR, GPR, and RFR, to predict BaTiO₃'s dielectric constant (D) based on 68 features, achieving a logarithmic error range within 50%. However, the prediction accuracy remains relatively low, falling short of high-precision goals. Based on the elemental information and basic properties of ABO₃ compounds, Lin *et al.*¹⁷ selected 42 features and utilized a Gradient Boosting Regressor (GBR) model for predicting the D of ABO₃ compounds, achieving an R² score of 0.887. Notably, Petousis *et al.*¹⁸ used Density Functional Perturbation Theory (DPFT) high-throughput calculations to predict D, which required a bandgap greater than 0.1 eV, a hull energy less than 0.02 eV, and atomic forces of the initial structure to be less than 0.05 eV/Å. Kim *et al.*¹⁹ reduced 275 features to 116 features, including 82 structural features, 30 chemical features, and four physical property features, identifying the bandgap as the most significant feature. Kireeva and Solov'ev²⁰ analyzed the influence of composition, process conditions, and crystal structure parameters on dielectric materials. Qin *et al.*²¹ developed low D microwave dielectric ceramics for 5G high-frequency communication applications. They identified seven key decorrelated features,

including unit cell Shannon entropy, dielectric polarization, average bond length, and unit cell volume occupied by a single atom. Morita *et al.*²² calculated a D value of 1346 and selected 93 features, which were input into the Support Vector Regression (SVR) model, to predict D, resulting in an R² score of 0.86.

The sure independence screening and sparsifying operator (SISSO) is a data-driven analysis method based on compressed sensing.²³ Based on the SISSO method and bond valence model, a new tolerance factor was proposed. Compared with the average area under curve (AUC) of the tolerance coefficient of 0.76, the new tolerance coefficient of 0.91 was achieved, which can better predict whether ABO₃ compounds have a perovskite structure, thus greatly improving the prediction accuracy.²⁴ A regression model was established to predict doped ABO₃ type perovskites, in which the SISSO method has a better effect on predicting the dielectric loss (tan δ).²⁵ A new tolerance factor τ was constructed to predict the stability of perovskite oxides and halides,²⁶ with significantly better results than the widely used Goldschmidt tolerance factor τ and the two-dimensional structure map using τ and octahedral factor μ. Chen *et al.*²⁷ also utilized SISSO to construct two accurate and easy-to-interpret descriptors for screening perovskite candidates with high forming probability.

This study employed machine learning (ML) models to determine the best descriptor for predicting the dielectric constant (D) and explore the correlation between the best descriptor and the D of ABO₃ type perovskites. The framework is outlined in Fig. 1. First, a dataset was constructed with 128 features from six distinct classes.

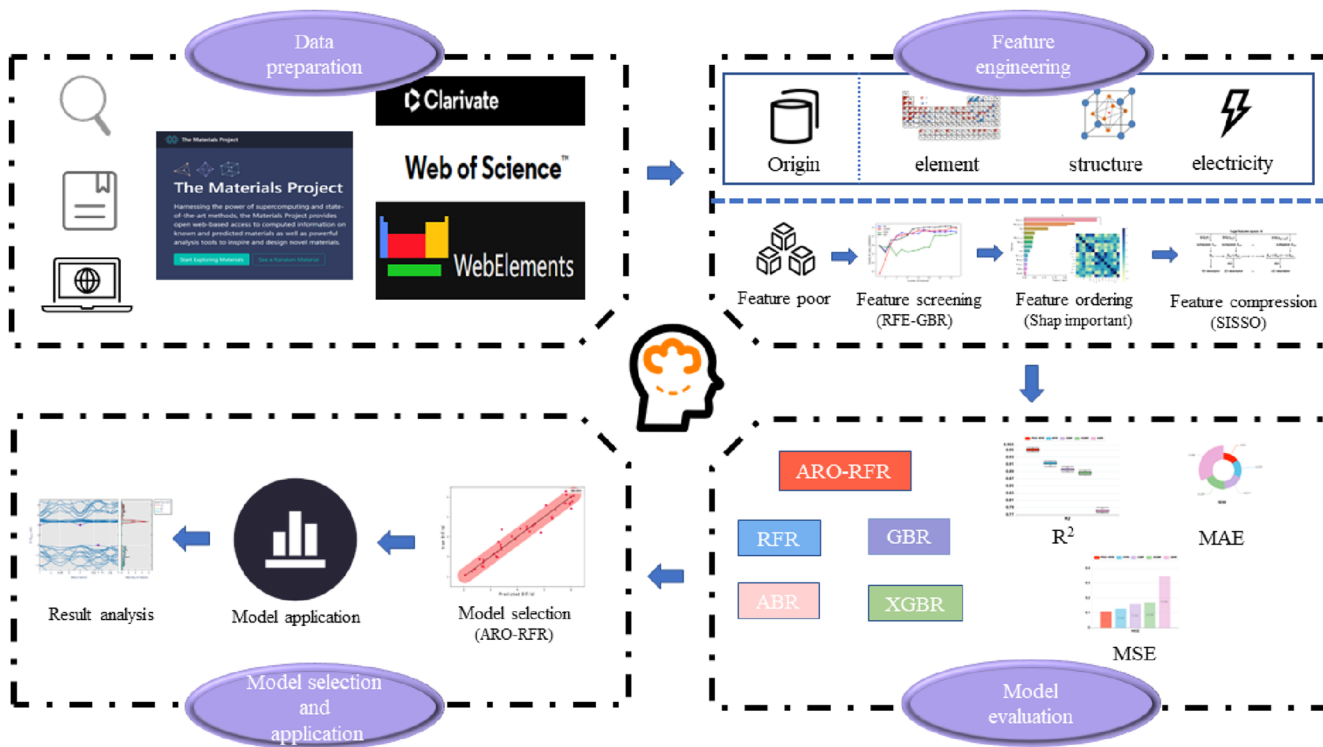


FIG. 1. Flowchart of this work.

Thirteen features were retained after feature selection using recursive feature elimination and cross-validation (RFECV), and three compound descriptors were created by SISSO's space reduction feature. Then the relationship between the descriptors and D was analyzed and explained using the Shapley additive interpretation (SHAP) technique. Compared with several kinds of ML regression models, the random forest regression (RFR) model with the best performance was selected and optimized by the Artificial Rabbits Optimization (ARO) algorithm.²⁸ Then the ARO-RFR model was evaluated for predicting the dielectric constant of ABO_3 compounds. Ultimately, two ABO_3 perovskites with potentially different D values were finally selected from 300 candidates. This framework helps us to discover new dielectric perovskite materials with desired D values. The general flow chart of the work is shown in Fig. 1.

II. METHODS

A. Generation of the dataset

In this work, the original feature dataset was sourced from Materials Project and WebElements,²⁹ as well as published references. The selected features of ABO_3 perovskites were divided into six categories, which ranged from energy to elements, such as density, volume, and atomic mass. In addition, these features encompassed thermodynamic and electronic properties, including ionization energy, electronegativity, electron affinity, and resistivity. The specific classification of these features is presented in Table S1 of the supplementary material. We collected 128 features from 204 ABO_3 compounds, randomly selecting 80% as the training set and 20% as the test set. In addition, we collected the dielectric constants of 300 unknown ABO_3 -type compounds as the prediction dataset.

B. Feature selection

Initially, 128 features were screened by recursive feature elimination cross-validation (RFECV) to eliminate irrelevant and

redundant features. Then, to identify the best regression model and determine the optimal number of features, five-fold cross-validation was conducted. Figure 2(a) illustrates the utilization of four built-in models—Random Forest Regression (RFR), Gradient Boosting Regression (GBR), Lightweight Gradient Boosting Regression (LGBMR), and Extreme Gradient Boosting Regression (XGBR) models—for feature screening and compared their performance scores. The results demonstrated that the GBR model exhibits superior predictive performance, surpassing other models significantly, with 13 features yielding the maximum R^2 score. Furthermore, Fig. 2(b) depicts the decreases in R^2 in the RFE-GBR model as the number of screened features increases. The 13 features selected are detailed in Table S2 of the supplementary material.

To analyze the closeness of relationship with the 13 features selected above, a Pearson correlation coefficient heat map was designed, as shown in Fig. 3. Blue and yellow represent the positive and negative correlation between the two features, respectively. In order to prevent the strong correlation among the selected features in batches and improve the generalization ability of the model, the features that have the most significant impact on D while exhibiting relatively low correlation with each other were identified and retained for prediction analysis.

Figure 3 shows that there was no significant correlation among the 13 features selected by RFE-GBR. To gain a deeper understanding of the individual impacts of these features on the predicted D, SHapley Additive exPlanations (SHAP) was employed to interpret the contribution of each feature to D. SHAP assigned a SHAP value to each feature in the sample, revealing the relationship between the feature and the predicted target D in the SHAP model as follows:

$$y = y_{base} + \sum_{i=1}^m \sum_{j=1}^n f(x_{ij}), \quad (1)$$

where y represents the SHAP value of the prediction model, y_{base} is the expected SHAP value of the model, and m and n denote the number of samples and the number of features, respectively. $f(x_{ij})$

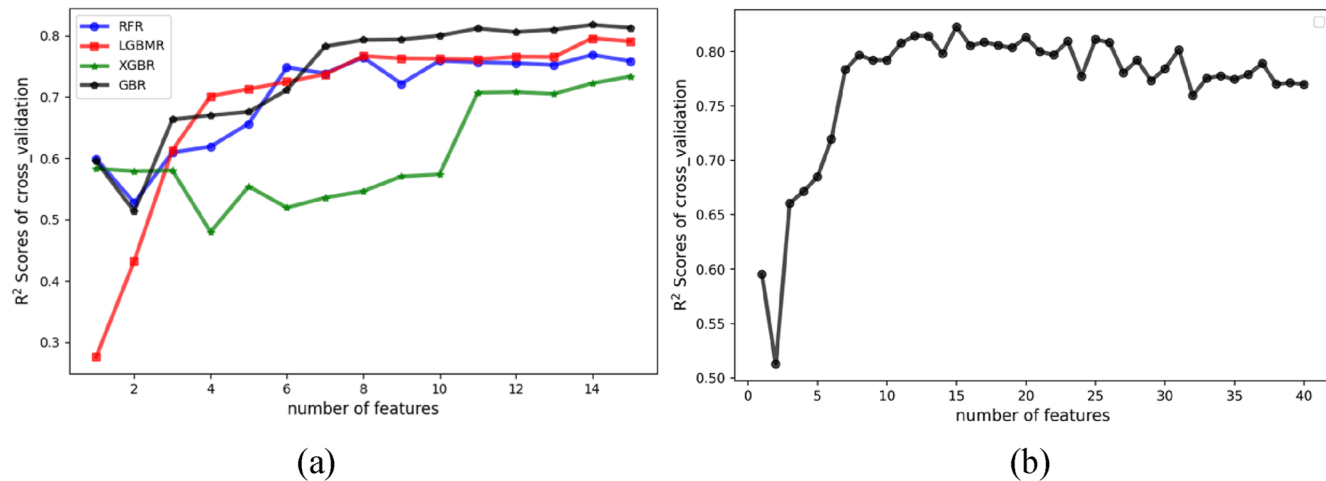


FIG. 2. (a) RFE, RFR, LGSMR, XGBR, and GBR were selected to determine the R^2 scores of the built-in model. (b) R^2 score under five-fold cross verification when GBR is selected in RFE.

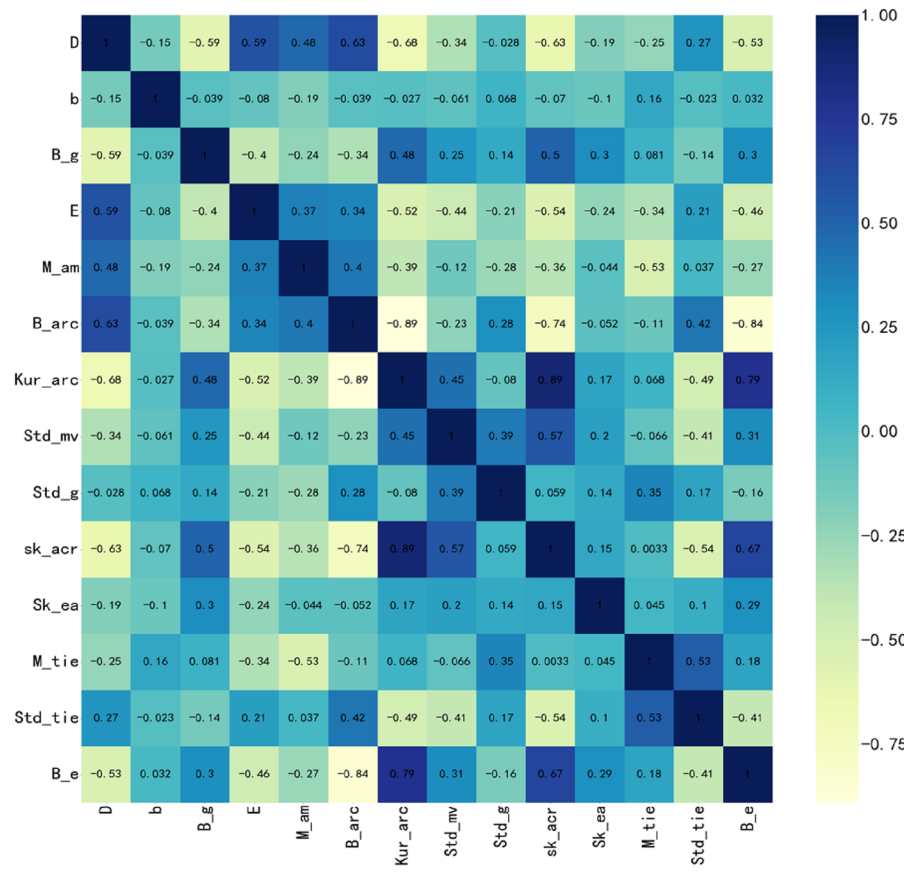


FIG. 3. Thermal maps of the Pearson correlation coefficient between 13 features and the dielectric constant screened by the RFE built-in model GBR.

signifies the SHAP value of the j th feature of the i th sample. When the SHAP value is greater than 0, it indicates that the feature positively contributes to improving the prediction value of the model, i.e., the feature plays a positive role in the multi-prediction model. Conversely, when the SHAP value is less than 0, it indicates that the feature plays an inverse role in the model.

The structural characteristics of the compound, such as cell parameter b , calculated radius, and molar volume, play a crucial role in determining the structural arrangement of the crystal. Wang *et al.*³⁰ highlighted that crystals with a highly symmetrical structural arrangement typically exhibit a low dielectric constant. As the calculated atomic radius increases, the interatomic distance may also expand, potentially leading to the formation of stronger electric dipoles, consequently higher dielectric constants.³¹ The electronegativity (B_e) disparity among elements influences the type and polarity of the chemical bond, subsequently affecting the degree of polarization and dielectric constant of the material. A significant electronegativity difference generally results in a higher dielectric constant. The electron affinity (SK_ea) of an element can impact the distribution of electrons in the compound, thereby influencing the degree of polarization and dielectric constant of the compound. The Fermi level (E) position in the compound directly

affects the conductive properties and polarization degree, consequently impacting D . A lower third ionization energy (Std_tie) may facilitate the formation of more positive ions in the compound, enhancing the material's polarization degree and yielding a higher D .

The 13 selected features were analyzed using the RFE-GBR algorithm using SHAP plots, ranking their impacts on the D of the perovskite. Figure 4(a) illustrates that the computed radius of the B-site (B_{arc}) exerts the most substantial impact on D . D is associated with the cutoff radius of electrostatic shielding and the radius of the local density of states, both of which are influenced by the computed B-site radius. Consequently, the selection of the computed B-site radius (B_{arc}) holds scientific significance. Moreover, B_{arc} , B-site electronegativity (B_e), standard deviation of third ionization energy at A/B/O sites (Std_tie), bandgap (B_g), b , and E are deemed the six most important features, aligning with the RFE screening results. Figure 4(b) indicates the effects of the 13 most important features on the dielectric constant D for all samples. The top three influential features were found to be B_{arc} , B_e , and Std_tie. In particular, for the most significant feature B_{arc} , samples with lower B_{arc} values tended to exhibit higher D as SHAP values at this point were more inclined to display large positive values, promoting

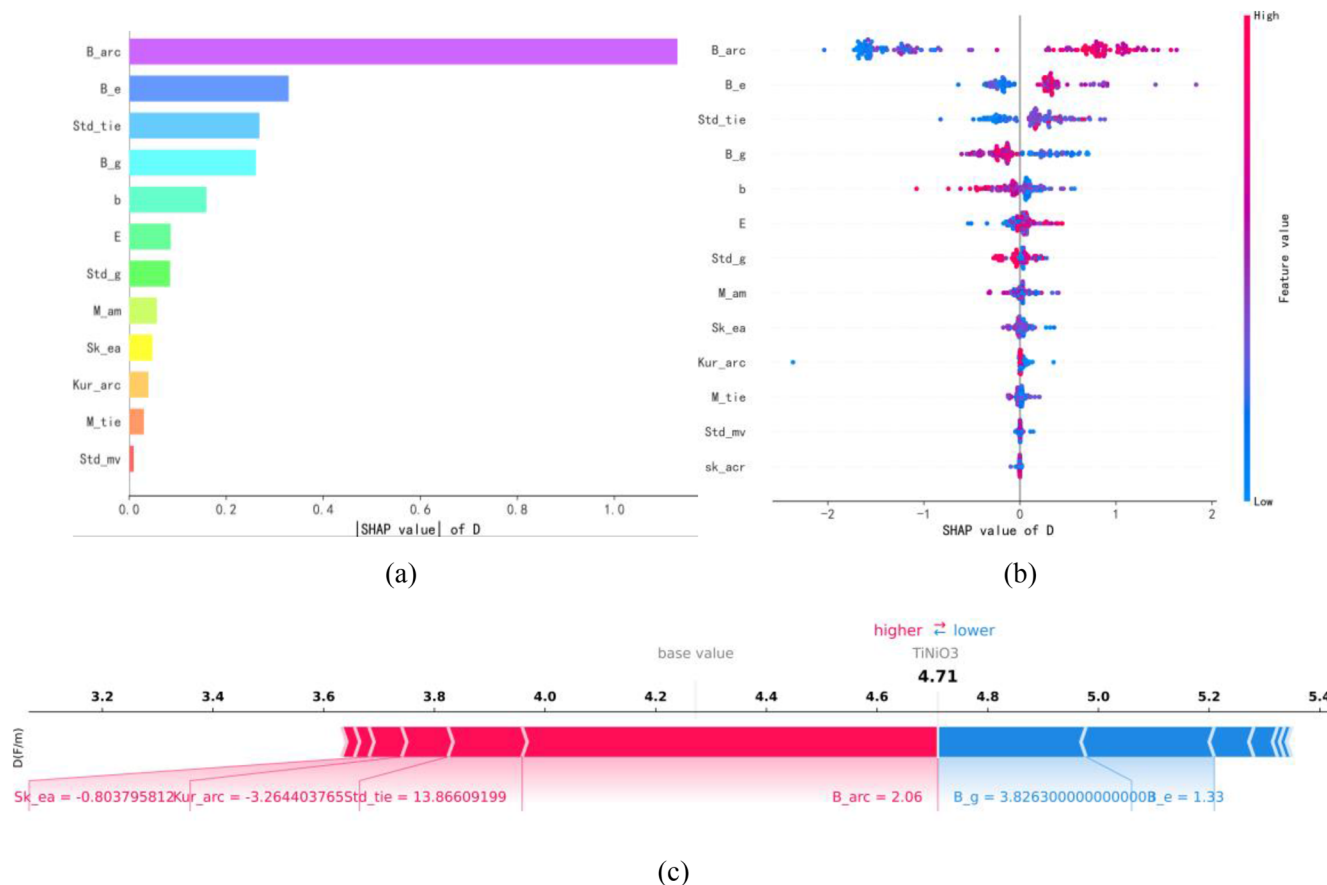


FIG. 4. (a) Feature importance under the SHAP model, where the x-axis represents the absolute average SHAP values of the features. (b) Global contributions of all samples according to SHAP, with purple and blue colors indicating the magnitude of feature values. (c) SHAP analysis of the local contributions of features for the sample TiNiO₃.

greater D. In addition, we analyzed the local influence of the optimal features by taking the sample TiNiO₃ as an example, elucidating the contribution of each feature to the final prediction, as depicted in Fig. 4(c). The average value across all samples was 4.25, while the predicted dielectric constant was 4.71. Here, the length of the arrows corresponds to the SHAP values of the features. Positive (red) and negative (blue) SHAP values represented the individual contributions of a single feature to D. The width of the color range indicated the feature's impact magnitude. Notably, B_{arc} achieved a feature weight of 2.06.

C. Model evaluation index

Four machine learning algorithms were employed to predict D of ABO₃ perovskites: adaptive enhanced regression tree model (ABR), extreme gradient lifting regression (XGBR), gradient enhanced regression (GBR), and random forest regression (RFR). The best model was selected based on the training and evaluation metrics, R², MAE, and MSE, where an R² closer to 1 and lower MAE or MSE indicate better performance. Their formulas are as follows:

$$R^2 = 1 - \frac{\sum_i (x_i - y_i)^2}{\sum_i (\bar{x}_i - x_i)^2}, \quad (2)$$

$$MAE = \frac{1}{m} \sum_{i=1}^m |(y_i - x_i)|, \quad (3)$$

$$MSE = \frac{1}{m} \sum_{i=1}^m (y_i - x_i)^2, \quad (4)$$

where x_i is the predicted dielectric constant D value of the compound, y_i is the true dielectric constant D value of the compound, \bar{x}_i is the mean of the dielectric constant, and m is the sample size. Using five-fold cross-validation and 13 selected features, the dielectric constants were predicted and analyzed. GridSearchCV was utilized to optimize each model to achieve the best prediction results.

D. Feature dimension reduction

The 13 selected features were divided into three groups: structural properties (three features), atomic size class (six features), and

TABLE I. Three categories of descriptors constructed by SISSO.

Classes	Correlation	Descriptor	Position
Structural attribute	0.6987	(B_g-E) + sin(b)	Figure 5(a) SISSO_a1
Atomic property	0.7149	abs(Kur_arc-sqrt(M_am))	Figure 5(b) SISSO_b1
Electrical property	0.24	abs((Sk_ea) ⁶ -(M_tie-B_e))	Figure 5(c) SISSO_c1

electrical properties (four features). To address potential redundancy among these features, the Sure Independence Screening and Sparsifying Operator (SISSO) approach was applied to compress the feature space and refine it to a low-dimensional descriptor with desired predictive information. SISSO begins by constructing an initial feature space integrating all potential features related to the target properties. It then autonomously identifies the optimal descriptor by combining features, thereby optimizing the feature space. The descriptor and their relationships are obtained through Eq. (5) as follows:

$$y = \beta_0 + \beta_1 x_1 + \beta_2 x_2 + \cdots + \beta_n x_n + \beta_{12} x_1 x_2 + \beta_{13} x_1 x_3 + \cdots + \beta_{ij} x_i x_j, \quad (5)$$

where y represents the target variable, x_1, \dots, x_n denotes the feature variables, β_0, \dots, β_n represents the corresponding coefficient, and $x_1 x_2, x_1 x_3, \dots, x_i x_j$ denotes the interaction between the descriptor. When β_0, \dots, β_n is 0, the solution of the equation is the best descriptor.

First, 90 descriptors of three classes were constructed, with each class having 30 descriptors. Then RFR model was used to traverse each constructed descriptor and screen out the one with the highest R^2 , as shown in Table I.

Figure 5 illustrates the descriptors constructed by SISSO and compared their contribution to D both before and after contribution. Ultimately, nine features were determined to be highly related to D, including three descriptors constructed by SISSO, Fermi level

E, B-position calculation radius (B_arc), standard deviation of molar volume at A, B, and O (Std_mv), standard deviation of the atomic group (Std_g), statistical skew of the calculated radius at A, B, and O (sk_acr), and standard deviation of the third ionization energy at A, B, and O (Std_tie). Detailed correlations between the three categories of SISSO-constructed descriptors and D are provided in Tables S3–S5 in the supplementary material.

In Fig. 5(a), the left semicircle denotes the input used to construct the descriptor of the structure class by SISSO, while the right semicircle illustrates the three descriptors constructed. Then the best structure class descriptor SISSO_a1 = (B_g-E) + sin(b), which exerts the greatest influence on perovskite D, was obtained by iterating through the right semicircle. Figure 5(b) mirrors Fig. 5(a), where the best atomic class descriptor SISSO_b1 = abs(Kur_arc-sqrt(M_am)) can be derived. From Fig. 5(c), the best electronic class descriptor SISSO_c1 = abs((Sk_ea)⁶-(M_tie-B_e)) was screened out. However, based on the contribution of the constructed descriptors for electrical properties to the target D shown in Table S5 of the supplementary material, the correlation was not as significant, as anticipated. An additional experiment was conducted without SISSO feature construction for electrical properties, leading to the elimination of related features of atomic and structural structures. Upon running the model, the R^2 score is 0.901. However, after participation with SISSO feature construction, the R^2 score improved to 0.951, enhancing the model's fitting performance. Therefore, SISSO was utilized to create electrical descriptors in this work, as illustrated in Fig. 5(c).

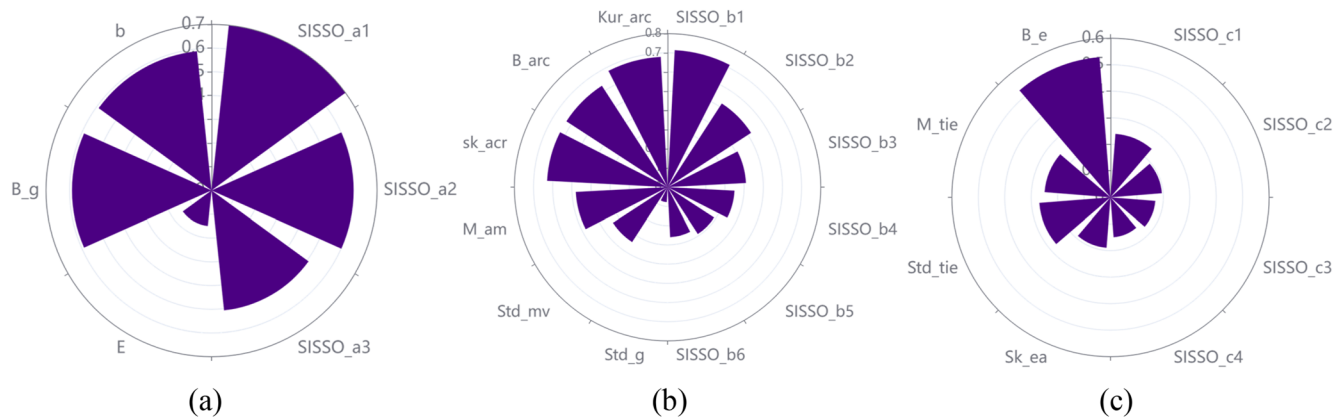


FIG. 5. (a) Comparison of the correlation between the three screened structural features and the SISSO structural description; (b) comparison of the six screened atom-like features and the SISSO structural description; (c) comparison of the four screened electrical properties and the SISSO structural description.

E. Model selection

In comparison to traditional decision trees and bagging learners, RFR incorporates random attribute selection, thereby enhancing the generalization performance of the final integrated model and yielding superior prediction results. However, considering the parameter optimization of the RFR model, a hybrid prediction model (ARO-RFR) was proposed. Compared with other algorithms, the Artificial Rabbits Optimization (ARO) algorithm can efficiently determine global optimal solutions for most unimodal, multimodal, and composite functions.

1. Artificial rabbits optimization model: ARO-RFR

A fusion prediction model ARO-RFR is presented in Fig. 6, which consists of a two-layer framework. The upper level was chiefly responsible for designing a suitable ARO-RF model to predict the D by finding the optimal parameters of the RFR model. The lower level focused on model optimization, employing ARO to transform the D solving problem under feature constraints into nonlinear optimization. Specifically, ARO was introduced to search the key parameters of the RFR model by fast global search. The optimization objective is to identify the features (B_arc, B_e, Std_tie, etc.). The performance index of D was optimized within the constraint range. In this paper, the integral of the absolute value of D error was selected as the estimation performance indicator to reflect the tracking performance of the optimal parameter, expressed as

$$J_k(\xi) \triangleq \sum_{k=0}^N |\tilde{X}_k(k, \xi)|. \quad (6)$$

Here, $|\tilde{X}_k(k, \xi)|$ represents the residual between the predicted value D and the actual value D^* in the kth iteration. By finding the minimum value of $J_k(\xi)$, a set of hyperparameters ξ is identified, under which the RFR model can optimize the prediction accuracy.

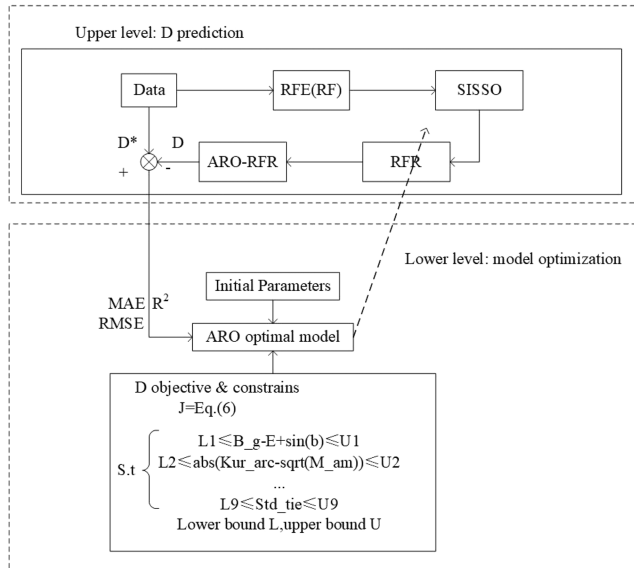


FIG. 6. Overall flow chart of model prediction.

2. Artificial rabbits optimization (ARO) algorithm

ARO is derived from the survival strategies of rabbits in nature, including detoured foraging and random hiding. The ARO algorithm uses the foraging and hiding strategies of real rabbits, switching between the two strategies through energy decline (see the Appendix in the supplementary material).

(1) Detour foraging:

$$\vec{v}_i(t+1) = \vec{x}_j(t) + R \cdot (\vec{x}_i(t) - \vec{x}_j(t)) \\ + \text{round}(0.5 \cdot (0.5 + r_1)) \cdot n_1, \quad i, j = 1, \dots, n \text{ and } j \neq i. \quad (7)$$

(2) Random hiding:

$$\vec{b}_{i,j}(t) = \vec{x}_i(t) + H \cdot g \cdot \vec{x}_i(t), \quad i = 1, \dots, n \text{ and } j = 1, \dots, d. \quad (8)$$

(3) Energy shrink:

$$A(t) = 4 \left(1 - \frac{t}{T}\right) \ln \frac{1}{r}. \quad (9)$$

Figure 7 shows the flow diagram of the entire algorithm. The artificial rabbits algorithm simulates the process of rabbits searching for food and escaping predators and seeks the optimal solution by iteratively optimizing the search space. Finally, the artificial rabbits algorithm will return an optimal combination of hyperparameters for training the final random forest model and evaluating the model's performance on a test set.

3. ARO-RFR hyperparameter optimization

Since the ARO algorithm focuses on identifying the optimal parameters of the RFR model, the R^2 score was evaluated as the

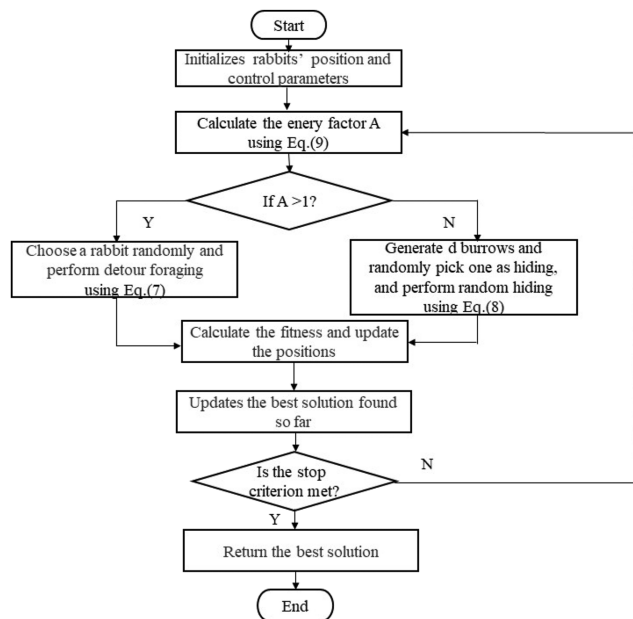


FIG. 7. Frame diagram of ARO-RFR.

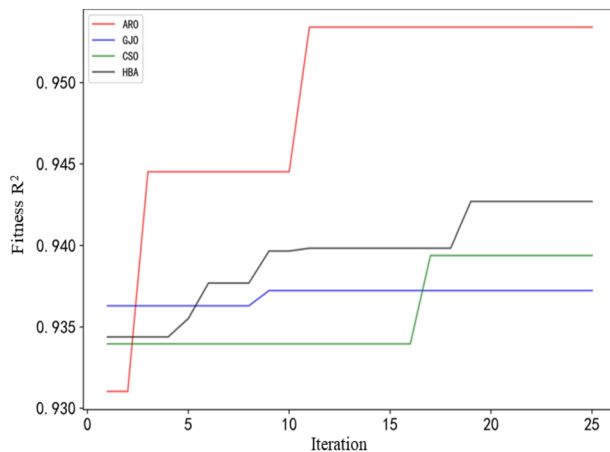


FIG. 8. Comparison of four optimization algorithms.

optimal parameter. After numerous iterations, the optimal parameters were successfully relayed back to the RFR model. Figure 8 shows the adaptive iterative graph for several optimization algorithms, including Golden Jackal Optimization (GJO), competitive

swarm optimizer (CSO), Honey Badger Algorithm (HBA) and ARO algorithm. Notably, the ARO algorithm stood out both in terms of the number of iterations and achieving the highest fitness value. Supplementary Table S6 in the [supplementary material](#) provides three optimal parameters of the ARO fitness value.

III. RESULT ANALYSIS

A. Prediction of dielectric constant D

Following the feature compression discussed in Sec. II C, final selection of nine features was made to predict D. Figures 9(a)–9(d) depict comparisons between actual and predicted D values for both the training and the test dataset using the four models of RFR, GBR, XGBR, and ABR, respectively. Among all these methods, the RFR model achieved the best fitting result with R^2 values of 0.91, MAE of 0.253, and MSE of 0.128 for both training and test sets, as illustrated in Fig. 10. Meanwhile, to avoid the RFR model from falling into the local optimum, it was further optimized using ARO, as outlined in Sec. II D. Figure 9(e) illustrates the fitting graph of ARO-RFR, which obviously clearly surpasses that of a solitary RFR model within the minimum error margin from the true value. Figures 10(a)–10(c) indicate that ARO optimization elevated the R^2 score of the RFR model to 0.95, an enhancement of 4.4% over the unoptimized scenario, reduced the MAE to 0.23, lower by 9.09%, and decreased

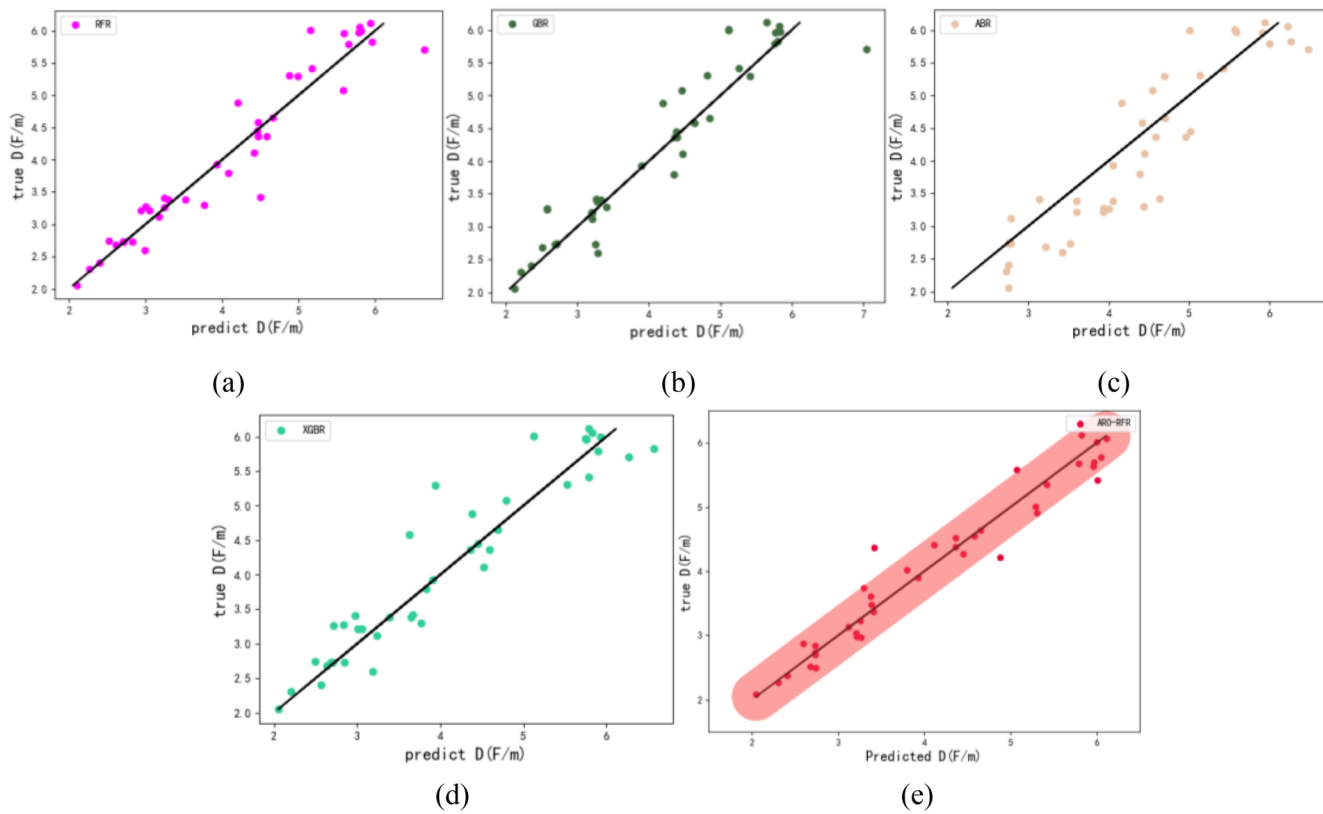


FIG. 9. (a)–(e) Predicted fitting graphs of the dielectric constant D by RFR, GBR, ABR, XGBR, and ARO-RFR models, respectively.

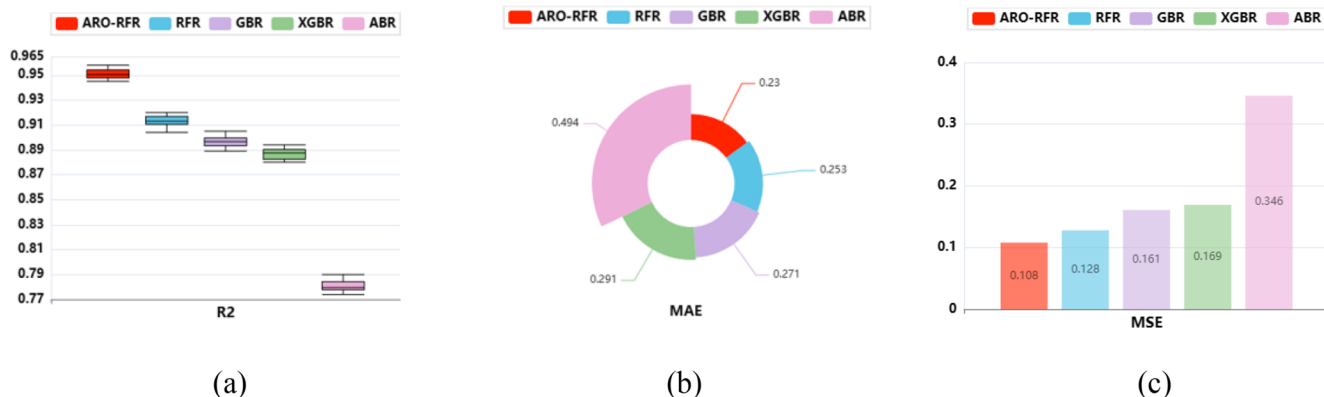


FIG. 10. (a)–(c) Comparison of R^2 , MAE, and MSE results of ARO-RFR, RFR, GBR, XGBR, and ABR models.

the MSE to 0.108, a reduction of 0.02. The results indicated that ARO considerably boosted the RFR model's performance in predicting D.

Table II compared the methodological and experimental results of this work with those from the literature.^{32,33} The nine descriptors selected in this paper for prediction of D were not previously identified by other researchers, highlighting the novelty of using the ARO algorithm to refine the RF prediction model. Consequently, compared to previous work, the method employed herein manifested significant improvement on R^2 , MAE, and RMSE. Moreover, the study showed that superior performance can be realized by reasonably balancing the number of descriptors.

In Ref. 32, five features were identified: atomic radius of the B-site element, absolute electronegativity of the B-site element, Pauling electronegativity of the A-site element, equilibrium van der Waals radius of the B-site element, and ionization energy of the B-site element. Ref. 33 selected six features: the cation radius of site A, the difference between Bader and formal charge of B ions, the molecular

TABLE II. Comparison with previous work.

Compare	Feature number	Model	R^2	MAE	MSE	RMSE
This work	9	ARO-RFR	0.95	0.23	0.10	0.31
Reference 32	5	SVR	0.88	7
Reference 33	6	PLS regression	0.67	0.63

dynamics model (RDF) of A-A, the molecular dynamics model (RDF) of B-B, the spectral data of site A, and the spectral data of site B.

B. Analysis of filter descriptors and dielectric constant D

Figure 11(a) shows the influence of the descriptors derived from the structural attribute and atomic size classes on the D

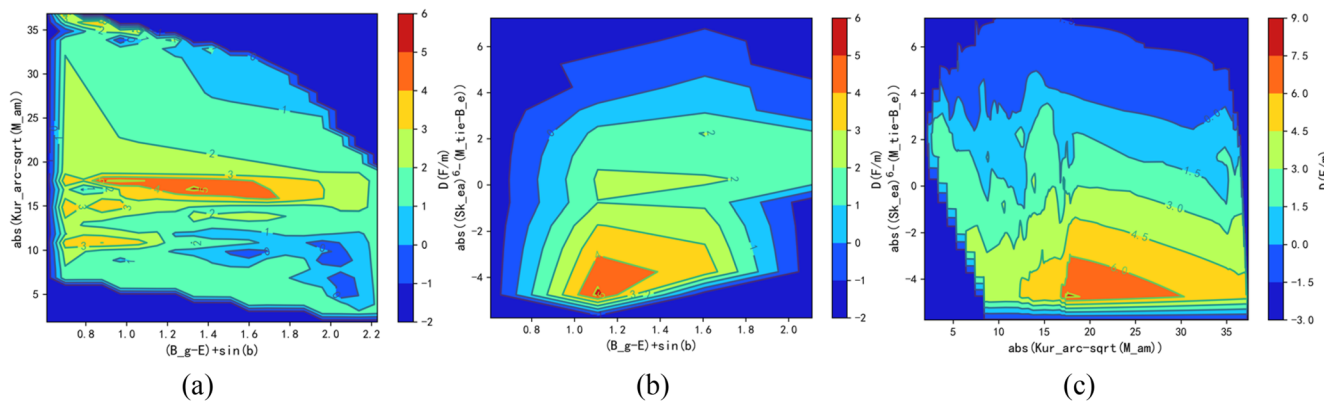


FIG. 11. (a)–(c) Relationship between the two descriptors constructed by SISMO and the dielectric constant D.

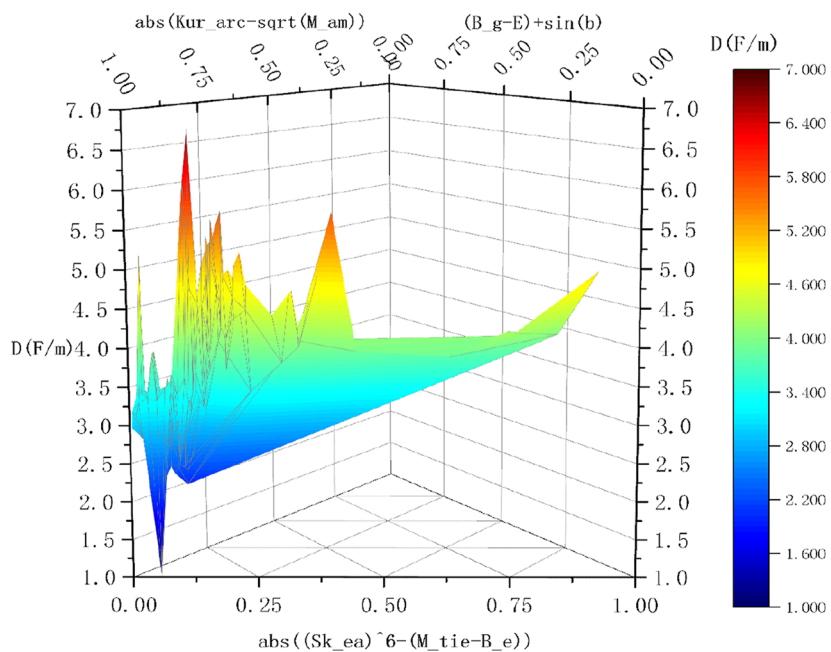
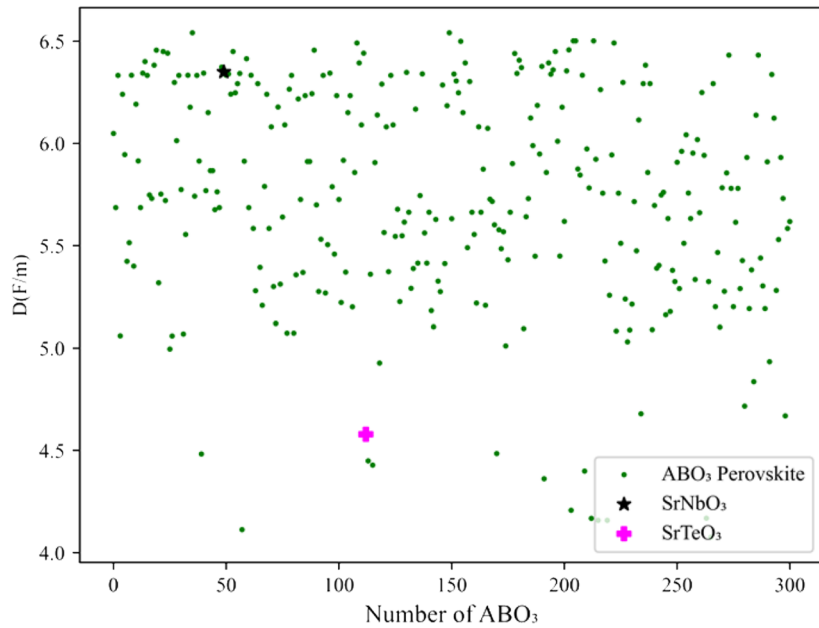


FIG. 12. Spatial distribution relationship between three constructed descriptors.

of ABO_3 perovskites. When $\text{abs}(\text{Kur_arc}-\sqrt{\text{M_am}})$ was clustered within ranges mentioned in Refs. 15 and 17 and $(\text{B}_g-\text{E}) + \sin(b)$ converged within the range of 1.0–1.7, the D of the ABO_3 perovskite was likely concentrated within the range of

[4.5, 5.6]. Figure 11(b) showed the dependency of D on descriptors between $\text{abs}((\text{Sk}_e\text{a})^6 - (\text{M}_t\text{i}\text{e} - \text{B}_e))$ and $(\text{B}_g-\text{E}) + \sin(b)$, with two regions of larger D separated by an apparent boundary at $-5 < \text{abs}((\text{Sk}_e\text{a})^6 - (\text{M}_t\text{i}\text{e} - \text{B}_e)) < -2$ and $1.05 < (\text{B}_g-\text{E}) + \sin(b) < 1.4$

FIG. 13. Predicted dielectric constants of 300 ABO_3 .

or $-5 < \text{abs}((\text{Sk_ea})^6 - (\text{M_tie-B_e})) < -3$ and $0.95 < (\text{B_g-E}) + \sin(\text{b}) < 1.7$. Figure 11(c) demonstrates that smaller $\text{abs}(\text{Kur_arc-sqrt}(\text{M_am}))$ with a value less than 8 and $\text{abs}((\text{Sk_ea})^6 - (\text{M_tie-B_e})) < 0$ or $\text{abs}((\text{Sk_ea})^6 - (\text{M_tie-B_e})) > 2$ should result in lower D. The constructed descriptors with the normalized representation are depicted in Fig. 12, illustrating the predicted D of the ABO_3 perovskite with different descriptors using the designed ARO-RFR model. It was observed that the high value of $(\text{B_g-E}) + \sin(\text{b})$ or $\text{abs}(\text{Kur_arc-sqrt}(\text{M_am}))$ and low value of $\text{abs}((\text{Sk_ea})^6 - (\text{M_tie-B_e}))$, which alternatively maintains $\text{abs}((\text{Sk_ea})^6 - (\text{M_tie-B_e}))$ and $\text{abs}(\text{Kur_arc-sqrt}(\text{M_am}))$ at certain levels, thus increasing the value of $(\text{B_g-E}) + \sin(\text{b})$, would increase electronic activity and cause structural change and exhibit a potentially higher dielectric constant of the ABO_3 -type perovskite.

IV. APPLICATION OF THE MODEL

Given the high prediction accuracy for D, it was used to predict the unknown D of 300 ABO_3 perovskites. Two compounds, SrNbO_3 and SrTeO_3 , were screened out, as shown in Fig. 13. The

black pentagram represents SrNbO_3 with a predicted D value of 6.54 (F/m), while the pink pentagram represents SrTeO_3 with a predicted D value of 3.57 (F/m). Figure 14(a) shows the predicted variation trend of D and energy band (B_g) using the ARO-RFR model, where D is inversely proportional to B_g. The experimental results also confirm the conclusion.^{34,35} For instance, as shown in Fig. 14(b), SrNbO_3 exhibited metallic properties due to the presence of d1 electrons, with its Fermi level situated within the conduction band. This grants electrons the ability to transition within the conduction band rather than through the conventional valence band to conduction band transition. This characteristic highlighted the unique advantage of metallic semiconductors, where electrons transition not from the valence band (VB) to the conduction band (CB), but within the conduction band itself, thereby enhancing its conductivity.³⁶ As shown in Fig. 14(c), the Fermi level was set at 0 eV, indicating its intersection with the energy bands, suggesting that these bands were partially filled. Electrons can move from occupied to empty energy levels, and partially filled bands imply that some electron states were occupied while others remained available for additional electrons. This attribute contributed to the conductivity of the compound SrTeO_3 .

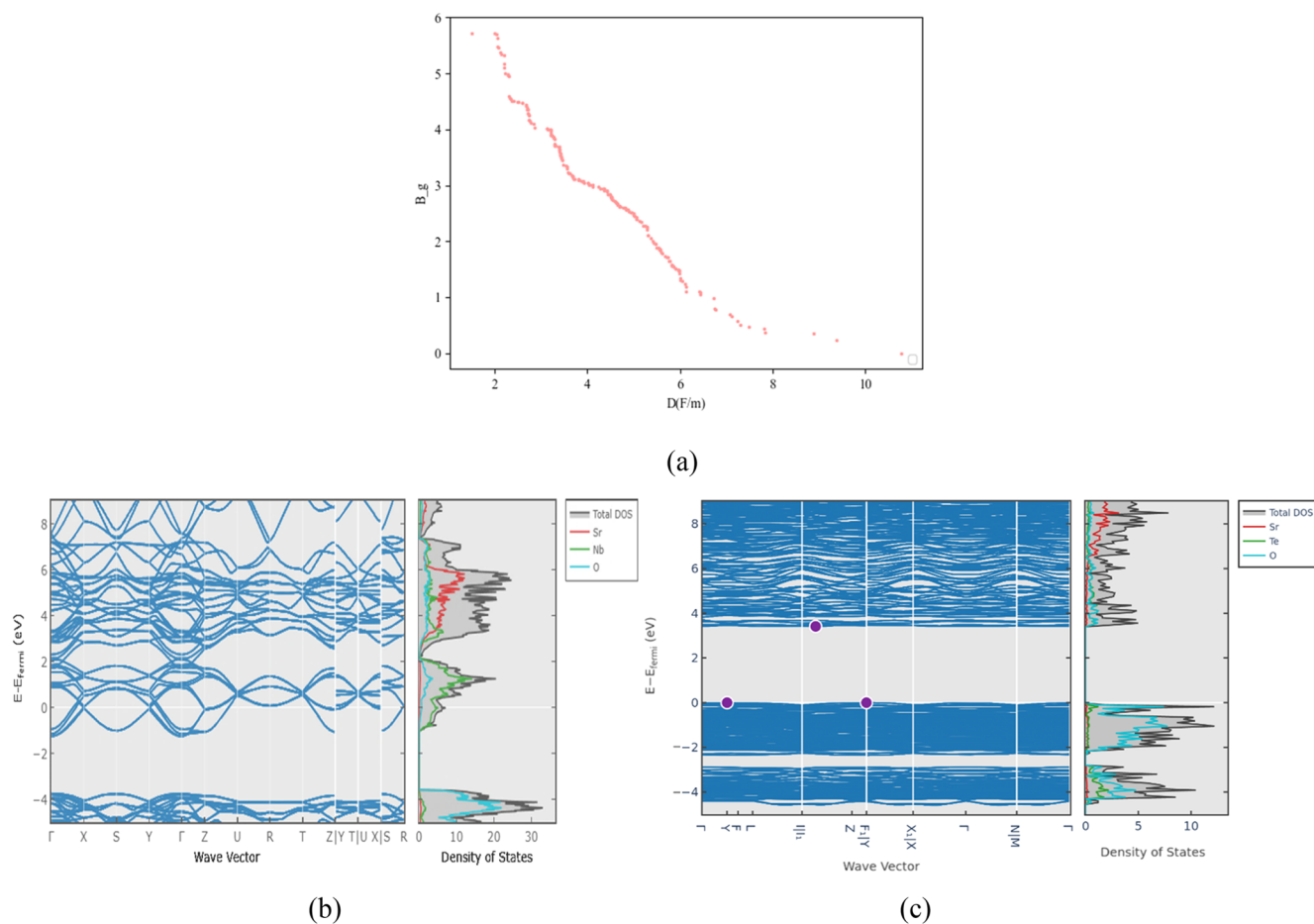


FIG. 14. (a) Relationship between B_g and D. (b) and (c) Band density diagram and wave vector diagram of SrNbO_3 and SrTeO_3 , respectively.

V. CONCLUSION

This study investigated the prediction of dielectric constant D of ABO_3 type perovskites using the data-driven approach. The Pearson correlation and SHAP method were combined to screen the main features, which were used to construct the descriptors more closely related to dielectricity. In addition, SISSO was applied to reduce the high dimensional features, resulting in the determination of nine descriptors that greatly influenced the D of the perovskite. By comparing multiple ML algorithms, the ARO algorithm was chosen to optimize the RFR model. Utilizing the hybrid ARO-RF prediction model led to improved performance, with the R^2 score reaching 0.95 and the MAE as low as 0.23. Finally, two perovskites, SrNbO_3 and SrTeO_3 , with different D values were successfully screened from 300 candidates. In conclusion, the proposed prediction framework effectively revealed the relationships between dielectric constant D and the identified descriptors of dielectric materials, aiding in the rapid identification of potential dielectricity of perovskites with different dielectric constants and offering guidance for further exploration of various properties of ABO_3 type perovskites.

SUPPLEMENTARY MATERIAL

See the [supplementary material](#) for the detailed feature lists, descriptors, and algorithms.

AUTHOR DECLARATIONS

Conflict of Interest

The authors have no conflicts to disclose.

Author Contributions

Taizhong Yao: Methodology (equal); Software (equal); Writing – original draft (equal). **Lanping Chen:** Writing – review & editing (equal). **Nan Hu:** Data curation (equal); Methodology (equal). **Lei Xu:** Data curation (equal). **Sichao Sun:** Data curation (equal).

DATA AVAILABILITY

The data that support the findings of this study are available within the article and its supplementary material.

REFERENCES

- ¹M. T. Sebastian, R. Ubic, and H. Jantunen, “Low-loss dielectric ceramic materials and their properties,” *Int. Mater. Rev.* **60**(7), 392–412 (2015).
- ²H. Yang, S. Zhang, H. Yang, Q. Wen, Q. Yang, L. Gui, Q. Zhao, and E. Li, “The latest process and challenges of microwave dielectric ceramics based on pseudo phase diagrams,” *J. Adv. Ceram.* **10**, 885–932 (2021).
- ³J. Fu, “High and temperature-stable dielectric constants in $\text{PNb}_2\text{O}_{25}$ ceramic,” *J. Am. Ceram. Soc.* **105**(6), 3740–3745 (2022).
- ⁴B. Xu, J. Iñiguez, and L. Bellaiche, “Designing lead-free antiferroelectrics for energy storage,” *Nat. Commun.* **8**(1), 15682 (2017).
- ⁵W. Li, J. Zheng, B. Hu *et al.*, “High-performance solar flow battery powered by a perovskite/silicon tandem solar cell,” *Nat. Mater.* **19**(12), 1326–1331 (2020).
- ⁶J. Li, Z. Shen, X. Chen *et al.*, “Grain-orientation-engineered multilayer ceramic capacitors for energy storage applications,” *Nat. Mater.* **19**(9), 999–1005 (2020).
- ⁷M. Acosta, N. Novak, V. Rojas *et al.*, “ BaTiO_3 -based piezoelectrics: Fundamentals, current status, and perspectives,” *Appl. Phys. Rev.* **4**(4), 041305 (2017).
- ⁸M. Monteagudo Honrubia, J. Matanza Domingo, F. J. Herraiz-Martínez, and R. Giannetti, “Low-cost electronics for automatic classification and permittivity estimation of glycerin solutions using a dielectric resonator sensor and machine learning techniques,” *Sensors* **23**(8), 3940 (2023).
- ⁹J. J. Urban, W. S. Yun, Q. Gu, and H. Park, “Synthesis of single-crystalline perovskite nanorods composed of barium titanate and strontium titanate,” *J. Am. Chem. Soc.* **124**(7), 1186–1187 (2002).
- ¹⁰C. Kim, G. Pilania, and R. Ramprasad, “Machine learning assisted predictions of intrinsic dielectric breakdown strength of ABX_3 Perovskites,” *J. Phys. Chem. Lett.* **120**(27), 14575–14580 (2016).
- ¹¹X. Wang, Y. Sheng, J. Ning *et al.*, “A critical review of machine learning techniques on thermoelectric materials,” *J. Phys. Chem. Lett.* **14**(7), 1808–1822 (2023).
- ¹²J. Qin, Z. Liu, M. Ma *et al.*, “Structure and microwave dielectric properties of gillespite-type $\text{ACuSi}_4\text{O}_{10}$ ($\text{A} = \text{Ca}, \text{Sr}, \text{Ba}$) ceramics and quantitative prediction of the $Q \times f$ value via machine learning,” *ACS Appl. Mater. Interfaces* **13**(15), 17817–17826 (2021).
- ¹³X. Fang, Z. Chen, Q. Ma *et al.*, “ $\text{A}_2\text{BB}'\text{X}_6/\text{ABX}_3$ -type high-performance perovskites screening based on ensemble learning and high throughput screening,” *Sol. Energy* **262**, 111795 (2023).
- ¹⁴L. Chen, N. Hu, T. Yao *et al.*, “Rapid screening B-site doping ferroelectric perovskite with high Curie temperature for electronic applications by a novel IDBO-RF approach,” *Mater. Today Commun.* **38**, 107939 (2024).
- ¹⁵L. Chen, X. Wang, W. Xia, and C. Liu, “PSO-SVR predicting for the Ehull of ABO_3 -type compounds to screen the thermodynamic stable perovskite candidates based on multi-scale descriptors,” *Comput. Mater. Sci.* **211**, 111435 (2022).
- ¹⁶Y. Umeda, H. Hayashi, H. Moriwake, and I. Tanaka, “Prediction of dielectric constants using a combination of first principles calculations and machine learning,” *Jpn. J. Appl. Phys.* **58**, SLLC01 (2019).
- ¹⁷X. Lin, C. Li, H. Hao *et al.*, “Accelerated search for ABO_3 -type the electronic contribution of polycrystalline dielectric constants by machine learning,” *Comput. Mater. Sci.* **193**, 110404 (2021).
- ¹⁸I. Petoudis, D. Mrdjénovich, E. Ballouz *et al.*, “High-throughput screening of inorganic compounds for the discovery of novel dielectric and optical materials,” *Sci. Data* **4**, 160134 (2017).
- ¹⁹E. Kim, J. Kim, and K. Min, “Prediction of dielectric constants of ABO_3 -type perovskites using machine learning and first-principles calculations,” *Phys. Chem. Chem. Phys.* **24**(11), 7050–7059 (2022).
- ²⁰N. Kireeva and V. P. Solov'ev, “Machine learning analysis of microwave dielectric properties for seven structure types: The role of the processing and composition,” *J. Phys. Chem. Solids* **156**, 110178 (2021).
- ²¹J. Qin, Z. Liu, M. Ma, and Y. Li, “Machine learning approaches for permittivity prediction and rational design of microwave dielectric ceramics,” *J. Materiomics* **7**(6), 1284–1293 (2021).
- ²²K. Morita, D. W. Davies, K. T. Butler, and A. Walsh, “Modeling the dielectric constants of crystals using machine learning,” *J. Chem. Phys.* **153**(2), 024503 (2020).
- ²³R. Ouyang, S. Curtarolo, E. Ahmetcik *et al.*, “SISSO: A compressed-sensing method for identifying the best low-dimensional descriptor in an immensity of offered candidates,” *Phys. Rev. Mater.* **2**(8), 083802 (2018).
- ²⁴H.-Q. Hu, S.-G. Wu, Z.-T. Guo *et al.*, “New tolerance factor based on SISSO and machine learning for predicting stability of perovskite structure,” *Chin. J. Nonferrous Met.* **30**(8), 1887–1894 (2020).
- ²⁵P. Xu, D. Chang, T. Lu *et al.*, “Search for ABO_3 type ferroelectric perovskites with targeted multi-properties by machine learning strategies,” *J. Chem. Inf. Model.* **62**, 5038 (2021).
- ²⁶C. J. Bartel, C. Sutton, B. R. Goldsmith *et al.*, “New tolerance factor to predict the stability of perovskite oxides and halides,” *Sci. Adv.* **5**, eaav0693 (2019).
- ²⁷L. Chen, W. Xia, and T. Yao, “Identifying descriptors for perovskite structure of composite oxides and inferring formability via low-dimensional described features,” *Comput. Mater. Sci.* **226**, 112216 (2023).

- ²⁸L. Wang, Q. Cao, Z. Zhang *et al.*, “Artificial rabbits optimization: A new bio-inspired meta-heuristic algorithm for solving engineering optimization problems,” *Eng. Appl. Artif. Intell.* **114**, 105082 (2022).
- ²⁹See <https://www.webelements.com> for WebElements.
- ³⁰L. Wang, J. Yang, W. Cheng, *et al.*, “Progress on polymer composites with low dielectric constant and low dielectric loss for high-frequency signal transmission,” *Front. Mater.* **8**, 774843 (2021).
- ³¹N. Šegatin, T. Pajk Žontar, and N. Poklar Ulrich, “Dielectric properties and dipole moment of edible oils subjected to ‘frying’ thermal treatment,” *Foods* **9**(7), 900 (2020).
- ³²Y. Ye, Z. Ni, K. Hu *et al.*, “Dielectric constant prediction of perovskite microwave dielectric ceramics via machine learning,” *Mater. Today Commun.* **35**, 105733 (2023).
- ³³Y. Noda, M. Otake, and M. Nakayama, “Descriptors for dielectric constants of perovskite-type oxides by materials informatics with first-principles density functional theory,” *Sci. Technol. Adv. Mater.* **21**(1), 92–99 (2020).
- ³⁴K. Yim, Y. Yong, J. Lee *et al.*, “Novel high- κ dielectrics for next-generation electronic devices screened by automated *ab initio* calculations,” *NPG Asia Mater.* **7**(6), e190 (2015).
- ³⁵O. Fursenko, J. Bauer, G. Lupina *et al.*, “Optical properties and band gap characterization of high dielectric constant oxides,” *Thin Solid Films* **520**(14), 4532–4535 (2012).
- ³⁶X. Xu, C. Randorn, P. Efstrathiou, and J. T. S. Irvine, “A red metallic oxide photocatalyst,” *Nat. Mater.* **11**(7), 595–598 (2012).

Supporting Information for

Discovering ABO₃-Type Perovskite with Different Dielectric Constant via Intelligent Optimization Algorithm

Taizhong Yao^a, Lanping Chen^{a,b*}, Nan Hu^b, Lei Xu^a, Sichao Sun^b

^aSchool of Microelectronics and Control Engineering, Changzhou University, Changzhou 213159, Jiangsu, China

^bSchool of Computer Science and Artificial Intelligence, Changzhou University, Changzhou 213159, Jiangsu, China

*Email: chenlp@cczu.edu.cn

Table S1 The meaning of features

Features	Abbreviation
Cell parameter a	a
Cell parameter b	b
Cell parameter c	c
Cell angle alpha	alpha
Cell angle beta	beta
Cell angle theta	theta
volume	V
nsites	Ns
number	Nu
density	D_a
Uncorrected energy per atom	U_epa
Energy per atom	E_pa
Formation energy per atom	F_epa
Energy above hull	E_ah
Band gap	B_g
efermi	E
A atomic mass	A_am
B atomic mass	B_am
The mean of atomic mass of A, B, and O positions	M_am
The Standard deviation of atomic mass of A, B, and O positions	Std_am
The Skewness of atomic mass of A, B, and O positions	Sk_am
The Kurtosis of atomic mass of A, B, and O positions	Kur_am
A atomic number	A_an
B atomic number	B_an
The mean of atomic number of A, B, and O positions	M_an
The Standard deviation of atomic number of A, B, and O positions	Std_an
The Skewness atomic number of A, B, and O positions	Sk_an

The Kurtosis atomic number of A, B, and O positions	Kur_an
A atomic radius calculated	A_arc
B atomic radius calculated	B_arc
The mean of atomic radius calculated of A, B, and O positions	M_arc
The Standard deviation of atomic radius calculated at A, B, and O positions	Std_arc
The Skewness of atomic radius calculated of A, B, and O positions	Sk_arc
The Kurtosis of atomic radius calculated of A, B, and O positions	Kur_arc
A max oxidation state	A_maxos
B max oxidation state	B_maxos
The mean of max oxidation state of A, B, and O positions	M_maxos
The Standard deviation of max oxidation state of A, B, and O positions	Std_maxos
The Skewness of max oxidation state of A, B, and O positions	Sk_maxos
The Kurtosis of max oxidation state of A, B, and O positions	Kur_maxos
A min oxidation state	A_minos
B min oxidation state	B_minos
The mean of min oxidation state of A, B, and O positions	M_minos
The Standard deviation of min oxidation state of A, B, and O positions	Std_minos
The Skewness of min oxidation state of A, B, and O positions	Sk_minos
The Kurtosis of min oxidation state of A, B, and O positions	Kur_minos
A molar volume	A_mv
B molar volume	B_mv
The mean of molar volume of A, B, and O positions	M_mv
The Standard deviation of molar volume of A, B, and O positions	Std_mv
The Skewness of molar volume of A, B, and O positions	Sk_mv
The Kurtosis of molar volume of A, B, and O positions	Kur_mv
A Electronegativity	A_e
B Electronegativity	B_e

The mean of Electronegativity of A, B, and O positions	M_e
The Standard deviation of Electronegativity of A, B, and O positions	Std_e
The Skewness of Electronegativity of A, B, and O positions	Sk_e
The Kurtosis of Electronegativity of A, B, and O positions	Kur_e
A van der waals radius	A_vdwr
B van der waals radius	B_vdwr
The mean of van der waals radius of A, B, and O positions	M_vdwr
The Standard deviation of van der waals radius of A, B, and O positions	Std_vdwr
The Skewness of van der waals radius of A, B, and O positions	Sk_vdwr
The Kurtosis of van der waals radius of A, B, and O positions	Kur_vdwr
The number of rows of A-place elements at the periodic table	A_r
The number of rows of B-place elements at the periodic table	B_r
The mean of row numbers of elements A, B, and O at the periodic table	M_r
The Standard deviation of the row numbers of elements A, B, and O at the periodic table	Std_r
The Skewness of the row numbers of elements A, B, and O at the periodic table	Sk_r
The kurtosis of the row numbers of elements A, B, and O at the periodic table	Kur_r
The number of group of A-place elements at the periodic table	A_g
The number of group of B-place elements at the periodic table	B_g
The mean of group numbers of elements A, B, and O at the periodic table	M_g
The Standard deviation of the group numbers of elements A, B, and O at the periodic table	Std_g
The Skewness of the group numbers of elements A, B, and O at the periodic table	Sk_g
The Kurtosis of the group numbers of elements A, B, and O at the periodic table	Kur_g
A average cationic radius	A_acr
B average cationic radius	B_acr

The mean of average cationic radius of elements A, B, and O	M_acr
The Standard deviation of average cationic radius of A, B, and O positions	Std_acr
The Skewness of average cationic radius of A, B, and O positions	Sk_acr
The Kurtosis of average cationic radius of A, B, and O positions	Kur_acr
A average anionic radius	A_aar
B average anionic radius	B_aar
The mean of average anionic radius of A, B, and O positions	M_aar
The Standard deviation of average anionic radius of A, B, and O positions	Std_aar
The Skewness of average anionic radius of A, B, and O positions	Sk_aar
The Kurtosis of average anionic radius of A, B, and O positions	Kur_aar
A average ionic radius	A_air
B average ionic radius	B_air
The mean of average ionic radius of A, B, and O positions	M_air
The Standard deviation of average ionic radius of A, B, and O positions	Std_air
The Skewness of average ionic radius of A, B, and O positions	Sk_air
The Kurtosis of average ionic radius of A, B, and O positions	Kur_air
A electrical resistivity	A_er
B electrical resistivity	B_er
The mean of electrical resistivity of A, B, and O positions	M_er
The Standard deviation of electrical resistivity of A, B, and O positions	Std_er
The Skewness of electrical resistivity of A, B, and O positions	Sk_er
The Kurtosis of electrical resistivity of A, B, and O positions	Kur_er
A electron affinity	A_ea
B electron affinity	B_ea
The mean of electron affinity of A, B, and O positions	M_ea
The Standard deviation of electron affinity of A, B, and O positions	Std_ea

The Skewness of electron affinity of A, B, and O positions	Sk_ea
The Kurtosis of electron affinity of A, B, and O positions	Kur_ea
A first ionization energy	A_fie
B first ionization energy	B_fie
The mean of first ionization energy of A, B, and O positions	M_fie
The Standard deviation of first ionization energy of A, B, and O positions	Std_fie
The Skewness of first ionization energy of A, B, and O positions	Sk_fie
The Kurtosis of first ionization energy of A, B, and O positions	Kur_fie
A second ionization energy	A_sie
B second ionization energy	B_sie
The mean of second ionization energy of A, B, and O positions	M_sie
The Standard deviation of second ionization energy of A, B, and O positions	Std_sie
The Skewness of second ionization energy of A, B, and O positions	Sk_sie
The Kurtosis of second ionization energy of A, B, and O positions	Kur_sie
A third ionization energy	A_tie
B third ionization energy	B_tie
The mean of third ionization energy of A, B, and O positions	M_tie
The Standard deviation of third ionization energy of A, B, and O positions	Std_tie
The Skewness of third ionization energy of A, B, and O positions	Sk_tie
The Kurtosis of third ionization energy of A, B, and O positions	Kur_tie
The mean of the valences of elements A, B, and O	M_n
The Standard deviation of the valences of elements A, B, and O	Std_n
The Skewness of the valences of elements A, B, and O	Sk_n
The kurtosis of the valences of elements A, B, and O	Kur_n

Table S2 The 13 best features selected by REF-GBR

Feature	Symbol	Implication
Structural attribute	b	Cell parameters along the y axis
	B_g	Band gap
	E	Fermi level
Atomic property	M_am	The average number of atoms
	B_arc	The calculated radius of the B atom
	Kur_arc	The A,B,O positions calculate the kurtosis of the radius
	Std_mv	Standard deviation of A,B,O molar volume
	Std_g	Group standard deviation at A,B,O positions
	Sk_acr	The A,B,O bits calculate the statistical skewness of the radius
Electrical property	SK_ea	A,B,O electron affinity
	M_tie	The average of the third ionization energies at A,B,O positions
	Std_tie	Standard deviation of the third ionization energy at A,B,O positions
	B_e	Electronegativity of the B position

Table S3 Structure class construct descriptor

	SISSO descriptor	correlation
SISSOa1	(B_g-E)+sin(b)	0.6987
SISSO	(sin(B_g)-cos(B_g))	0.6772
SISSO	cos((E- B_g))	0.6609

Table S4 Atomic class construction descriptor

	SISSO descriptor	correlation
SISSO b1	abs(Kur_arc-sqrt(M_am))	0.7149
SISSOb2	(exp(-Std_mv)/(M_am*sk_acr))	0.32
SISSOb3	(cos(Std_g)*sin(Std_g))	0.31
SISSOb4	((B_arc-Std_mv)/cos(B_arc))	0.29
SISSOb5	((Std_g/sk_acr)*sin(Std_g))	0.27
SISSOb6	(abs(B_arc-Std_mv)/cos(B_arc))	0.26

Table S5 Electrical property construction descriptor

	SISSO descriptor	correlation
SISSOc1	abs((Sk_ea)^6-(M_tie-B_e))	0.24
SISSOc2	((Std_tie)^-1/cos(M_tie))	0.205
SISSOc3	((B_e)^-1/cos(Sk_ea))	0.204
SISSOc4	((M_tie/Std_tie)/cos(M_tie))	0.17

Artificial rabbits optimization algorithm

The ARO algorithm is inspired by the survival strategies of rabbits in nature, including departs for food and random hiding. The ARO algorithm uses the foraging and hiding strategies of real rabbits, switching between the two strategies through energy decline.

Detour foraging. When foraging for food, rabbits look far away and ignore things that are close at hand. They only graze randomly in other areas, not in their own area, and we call this foraging behavior roundabout foraging. In ARO, it is assumed that each rabbit in the colony has its own area, with some meadows and burrows, and rabbits always visit each other's locations randomly for foraging. The ARO's circumferential foraging behavior suggests that each searching individual tends to update its position and increase perturbation to another randomly selected searching individual in the group.

$$\vec{v}_i(t+1) = \vec{x}_j(t) + R \cdot (\vec{x}_i(t) - \vec{x}_j(t)) + \text{round}(0.5 \cdot (0.5 + r_1)) \cdot n_1,$$

$$i, j = 1, \dots, n \text{ and } j \neq i \quad (1)$$

$$R = L \cdot c \quad (2)$$

$$L = (e - e^{(\frac{t-1}{T})^2}) \cdot \sin(2\pi r_2) \quad (3)$$

$$c(k) = \begin{cases} 1 & \text{if } k == g(l) \\ 0 & \text{else} \end{cases} \quad k = 1, \dots, d \text{ and } l = 1, \dots, [r_3 \cdot d] \quad (4)$$

$$g = \text{randperm}(d) \quad (5)$$

$$n_1 \sim N(0,1) \quad (6)$$

Where, $\vec{v}_i(t+1)$ is the candidate position of rabbit i at time $t+1$, $\vec{x}_i(t)$ is the position of rabbit i at time t , n is the size of the number of rabbits, d is the dimension of the problem, T is the maximum number of iterations, $[\cdot]$ is the upper limit function, round represents rounding. $\text{randperm}(d)$ returns a random arrangement of integers from 1 to d , where r_1, r_2 and r_3 are the three random numbers in $(0,1)$, L is the run length, representing the movement speed when performing a roundabout foraging, and n_1 follows the standard normal distribution.

Perturbation in formula (1) helps ARO avoid local extremes and perform a global search. Running length L according to equation (3) can generate longer steps during the initial iteration. This length can result in shorter steps in later iterations. c is a mapping vector that helps the algorithm to randomly select a random number of elements to search for individuals to mutate during the foraging behavior. r stands for running operator, used to simulate the running characteristics of rabbits.

Random hiding. To avoid predators, rabbits usually dig a number of different burrows around their nests to hide. In ARO, in each iteration, a rabbit always generates d burrows around it along each dimension of the search space, and it always randomly chooses one of all burrows to hide to reduce the probability of predation. The following equation is given in this regard. The j burrow of rabbit i was formed by the following factors:

$$\vec{b}_{i,j}(t) = \vec{x}_i(t) + H \cdot g \cdot \vec{x}_i(t), i = 1, \dots, n \text{ and } j = 1, \dots, d \quad (7)$$

$$H = \frac{T-t+1}{T} \cdot r_4 \quad (8)$$

$$n_2 \sim N(0,1) \quad (9)$$

$$g(k) = \begin{cases} 1 & \text{if } k == j \\ 0 & \text{else} \end{cases} \quad k = 1, \dots, d \quad (10)$$

According to formula 7, d hole is generated in the rabbit's neighborhood along each dimension. H is the hidden parameter that linearly decreases from 1 to $1/T$ with random perturbations during iteration. Initially these burrows were created in a larger neighborhood of the rabbit, which decreased as the number of iterations increased.

As mentioned above, rabbits are often chased and attacked by predators. In order to survive, rabbits need to find a safe place to hide. Therefore, they refuse to choose a random cave from the cave to hide in order to avoid being caught. In order to model this random hiding strategy mathematically, the following equation is proposed:

$$\vec{v}_i(t+1) = \vec{x}_i(t) + R \cdot (r_4 \cdot \vec{b}_{i,r}(t) - \vec{x}_i(t)), i = 1, \dots, n \quad (11)$$

$$g_r(k) = \begin{cases} 1 & \text{if } k == \lceil r_5 \cdot d \rceil \\ 0 & \text{else} \end{cases} \quad k = 1, \dots, d \quad (12)$$

$$\vec{b}_{i,r}(t) = \vec{x}_i(t) + H \cdot g_r \cdot \vec{x}_i(t) \quad (13)$$

Where $\vec{b}_{i,r}(t)$ represents a randomly selected hole to avoid its d holes, and r_4, r_5 are two random numbers in $(0,1)$. According to formula 11, the i -th rabbit will attempt to update its position towards a randomly selected burrow from its d burrows.

After implementing one of the foraging and random hiding strategies, the rabbit's position is updated to Formula 14:

$$\vec{x}_i(t+1) = \begin{cases} \vec{x}_i(t) & f(\vec{x}_i(t)) \leq f(\vec{v}_i(t+1)) \\ \vec{v}_i(t+1) & f(\vec{x}_i(t)) > f(\vec{v}_i(t+1)) \end{cases} \quad (14)$$

In ARO, rabbits tend to perform frequent foraging in the initial phase of the iteration and frequent random hiding in the later phase of the iteration. This search mechanism stems from the rabbit's energy, which diminishes over time. Therefore, an energy factor was designed to simulate the transition from exploration to extraction. The energy factor of ARO is defined as follows:

$$A(t) = 4 \left(1 - \frac{t}{T} \right) \ln \frac{1}{r} \quad (15)$$

Where r is the random number in $(0,1)$. Therefore, in ARO, when the energy factor $A(t) > 1$, rabbits tend to randomly explore the areas of different rabbits for food during the exploration phase, thus detour foraging occurs. When the energy factor $A(t) \leq 1$, rabbits tend to randomly use their burrows in the utilization stage, resulting in random hiding.

Table S6 Three global optimal solutions under the most adaptive values of iteration

ARO-RFR optimized parameter	Global optimal solution
n_estimators	73
max_depth	97
random_state	71